

# **Nano-Hexapod - Test Bench**

Dehaeze Thomas

February 12, 2025

# Contents

<b>1 Nano-Hexapod Assembly Procedure</b>	<b>4</b>
<b>2 Suspended Table</b>	<b>7</b>
2.1 Introduction . . . . .	7
2.2 Experimental Setup . . . . .	7
2.3 Modal analysis of the suspended table . . . . .	8
2.4 Multi-body Model of the suspended table . . . . .	8
<b>3 Nano-Hexapod Measured Dynamics</b>	<b>10</b>
3.1 Modal analysis . . . . .	11
3.2 Identification of the dynamics . . . . .	11
3.3 Effect of payload mass on the dynamics . . . . .	13
<b>4 Nano-Hexapod Model Dynamics</b>	<b>16</b>
4.1 Nano-Hexapod model dynamics . . . . .	16
4.2 Dynamical coupling . . . . .	17
4.3 Effect of payload mass . . . . .	17
<b>5 Conclusion</b>	<b>21</b>

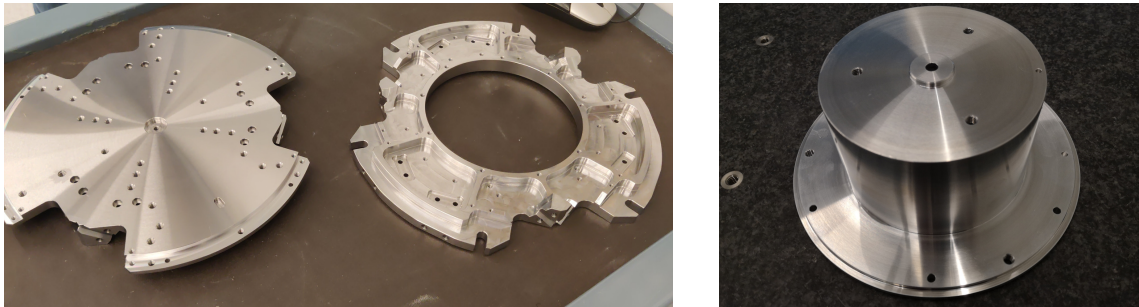
Prior to the nano-hexapod assembly, all the struts were mounted and individually characterized. In Section 1, the assembly procedure of the nano-hexapod is presented.

To identify the dynamics of the nano-hexapod, a special suspended table was developed, which consisted of a stiff “optical breadboard” suspended on top of four soft springs. The Nano-Hexapod was then mounted on top of the suspended table such that its dynamics is not affected by complex dynamics except from the suspension modes of the table that can be well characterized and modeled (Section 2).

The obtained nano-hexapod dynamics is analyzed in Section 3, and compared with the multi-body model in Section 4.

# 1 Nano-Hexapod Assembly Procedure

The assembly of the nano-hexapod is critical for both avoiding additional stress in the flexible joints (that would result in a loss of stroke) and for precisely determining the Jacobian matrix. The goal was to fix the six struts to the two nano-hexapod plates (shown in Figure 1.1a) while the two plates were parallel and aligned vertically so that all the flexible joints did not experience any stress. To do so, a precisely machined mounting tool (Figure 1.1b) is used to position the two nano-hexapod plates during the assembly procedure.



(a) Top and bottom plates

(b) Mounting tool

**Figure 1.1:** Nano-Hexapod plates (a) and mounting tool used to position the two plates during assembly (b)

The mechanical tolerances of the received plates were checked using a FARO arm<sup>1</sup> (Figure 1.2a) and were found to comply with the requirements<sup>2</sup>. The same was done for the mounting tool<sup>3</sup>. The two plates were then fixed to the mounting tool, as shown in Figure 1.2b. The main goal of this “mounting tool” is to position the flexible joint interfaces (the “V” shapes) of both plates so that a cylinder can rest on the 4 flat interfaces at the same time.

The quality of the positioning can be estimated by measuring the “straightness” of the top and bottom “V” interfaces. This corresponds to the diameter of the smallest cylinder which contains all points along the measured axis. This was again done using the FARO arm, and the results for all six struts are summarized in Table 1.1. The straightness was found to be better than  $15\ \mu\text{m}$  for all struts<sup>4</sup>, which is sufficiently good to not induce significant stress of the flexible joint during assembly.

The encoder rulers and heads were then fixed to the top and bottom plates, respectively (Figure 1.3), and the encoder heads were aligned to maximize the received contrast.

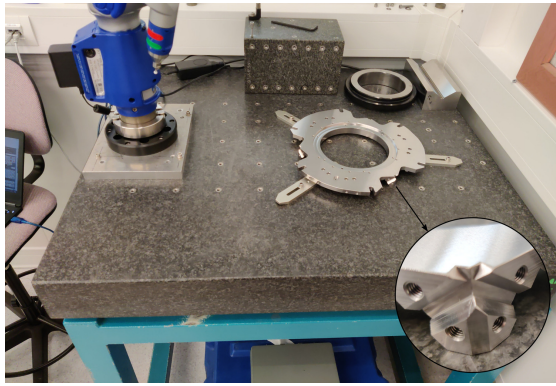
The six struts were then fixed to the bottom and top plates one by one. First, the top flexible joint is

<sup>1</sup>FARO Arm Platinum 4ft, specified accuracy of  $\pm 13\ \mu\text{m}$

<sup>2</sup>Location of all the interface surfaces with the flexible joints were checked. The fittings (182H7 and 24H8) with the interface element were also checked.

<sup>3</sup>The height dimension is better than  $40\ \mu\text{m}$ . The diameter fitting of 182g6 and 24g6 with the two plates is verified.

<sup>4</sup>As the accuracy of the FARO arm is  $\pm 13\ \mu\text{m}$ , the true straightness is probably better than the values indicated. The limitation of the instrument is here reached.



(a) Dimensional check of the bottom plate



(b) Wanted coaxiality between interfaces

**Figure 1.2:** A FARO arm is used to dimensionally check the received parts (a) and after mounting the two plates with the mounting part (b)

**Table 1.1:** Measured straightness between the two “V” shapes for the six struts. These measurements were performed twice for each strut.

Strut	Meas 1	Meas 2
1	7 $\mu m$	3 $\mu m$
2	11 $\mu m$	11 $\mu m$
3	15 $\mu m$	14 $\mu m$
4	6 $\mu m$	6 $\mu m$
5	7 $\mu m$	5 $\mu m$
6	6 $\mu m$	7 $\mu m$



(a) Encoder rulers



(b) Encoder heads

**Figure 1.3:** Mounting of the encoders to the Nano-hexapod. The rulers are fixed to the top plate (a) while encoders heads are fixed to the bottom plate (b)

fixed so that its flat reference surface is in contact with the top plate. This step precisely determines the position of the flexible joint with respect to the top plate. The bottom flexible joint is then fixed. After mounting all six struts, the mounting tool (Figure 1.1b) can be disassembled, and the nano-hexapod as shown in Figure 1.4 is fully assembled.

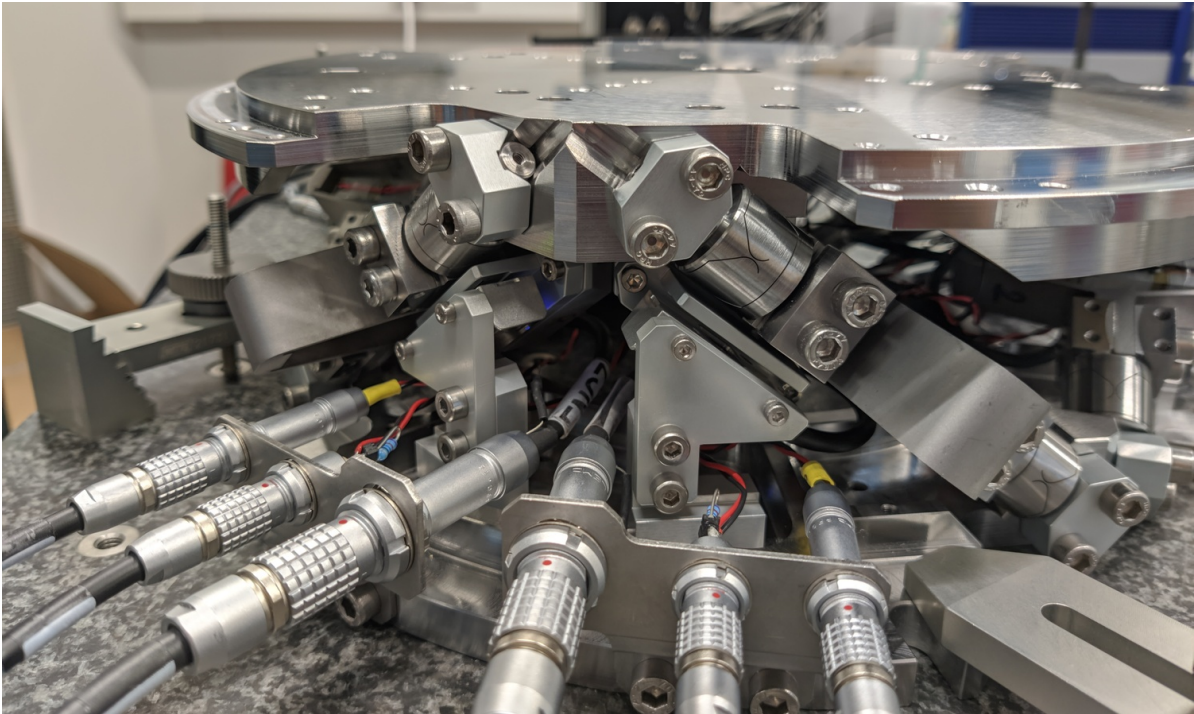


**Figure 1.4:** Mounted Nano-Hexapod

## 2 Suspended Table

### 2.1 Introduction

When a dynamical system is fixed to a support (such as a granite or an optical table), its dynamics will couple to the support dynamics. This may result in additional modes appearing in the system dynamics, which are difficult to predict and model. To prevent this issue, the strategy adopted here is to mount the nano-hexapod on top of a suspended table with low frequency suspension modes.

In this case, the modes of the suspended table were chosen to be at much lower frequency than those of the nano-hexapod such that good decoupling is obtained. Another key advantage is that the suspension modes of the table can be easily represented using a multi-body model. Therefore, the measured dynamics of the nano-hexapod on top of the suspended table can be compared to a multi-body model representing the same experimental conditions. The model of the Nano-Hexapod can thus be precisely tuned to match the measured dynamics.

The developed suspended table is described in Section 2.2. The modal analysis of the table is done in 2.3. Finally, the multi-body model representing the suspended table was tuned to match the measured modes (Section 2.4).

### 2.2 Experimental Setup

The design of the suspended table is quite straightforward. First, an optical table with high frequency flexible mode was selected<sup>1</sup>. Then, four springs<sup>2</sup> were selected with low spring rate such that the suspension modes are below 10Hz. Finally, some interface elements were designed, and mechanical lateral mechanical stops were added (Figure 2.1).

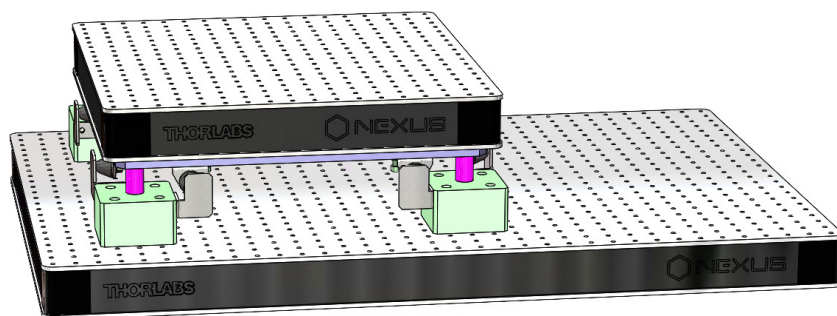


**Figure 2.1:** CAD View of the vibration table. The purple cylinders are representing the soft springs.

<sup>1</sup>The 450 mm x 450 mm x 60 mm Nexus B4545A from Thorlabs.

<sup>2</sup>“SZ8005 20 x 044” from Steinel. The spring rate is specified at  $17.8 N/mm$

## 2.3 Modal analysis of the suspended table

In order to perform a modal analysis of the suspended table, a total of 15 3-axis accelerometers<sup>3</sup> were fixed to the breadboard. Using an instrumented hammer, the first 9 modes could be identified and are summarized in Table 2.1. The first 6 modes are suspension modes (i.e. rigid body mode of the breadboard) and are located below 10Hz. The next modes are the flexible modes of the breadboard as shown in Figure 2.3, and are located above 700Hz.

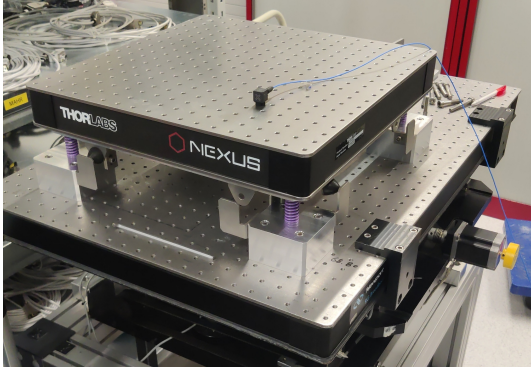


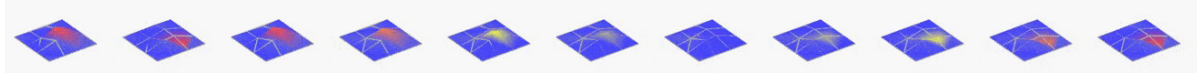
**Figure 2.2:** Mounted suspended table. Only 1 or the 15 accelerometer is mounted on top

**Table 2.1:** Obtained modes of the suspended table

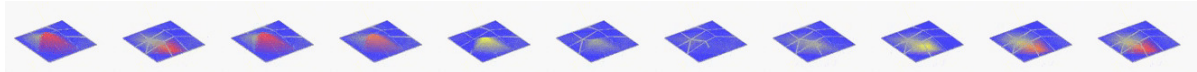
Modes	Frequency	Description
1,2	1.3 Hz	X-Y translations
3	2.0 Hz	Z rotation
4	6.9 Hz	Z translation
5,6	9.5 Hz	X-Y rotations
7	701 Hz	“Membrane” Mode
8	989 Hz	Complex mode
9	1025 Hz	Complex mode



(a) Flexible mode at 701Hz



(b) Flexible mode at 989Hz



(c) Flexible mode at 1025Hz

**Figure 2.3:** Three identified flexible modes of the suspended table

## 2.4 Multi-body Model of the suspended table

The multi-body model of the suspended table consists simply of two solid bodies connected by 4 springs. The 4 springs are here modeled with “bushing joints” that have stiffness and damping properties in x, y, and z directions.

The model order is 12, which corresponds to the 6 suspension modes. The inertia properties of the parts

<sup>3</sup>PCB 356B18. Sensitivity is 1 V/g, measurement range is  $\pm 5g$  and bandwidth is 0.5 to 5 kHz.

were determined from the geometry and material densities. The stiffness of the springs was initially set from the datasheet nominal value of  $17.8\text{ N/mm}$  and then reduced down to  $14\text{ N/mm}$  to better match the measured suspension modes. The stiffness of the springs in the horizontal plane is set at  $0.5\text{ N/mm}$ . The obtained suspension modes of the multi-body model are compared with the measured modes in Table 2.2.

**Table 2.2:** Comparison of suspension modes of the multi-body model and the measured ones

Directions	$D_x, D_y$	$R_z$	$D_z$	$R_x, R_y$
Multi-body	1.3 Hz	1.8 Hz	6.8 Hz	9.5 Hz
Experimental	1.3 Hz	2.0 Hz	6.9 Hz	9.5 Hz

### 3 Nano-Hexapod Measured Dynamics

The Nano-Hexapod was then mounted on top of the suspended table, as shown in Figure 3.1. All instrumentation (Speedgoat with ADC, DAC, piezoelectric voltage amplifiers and digital interfaces for the encoder) were configured and connected to the nano-hexapod using many cables.

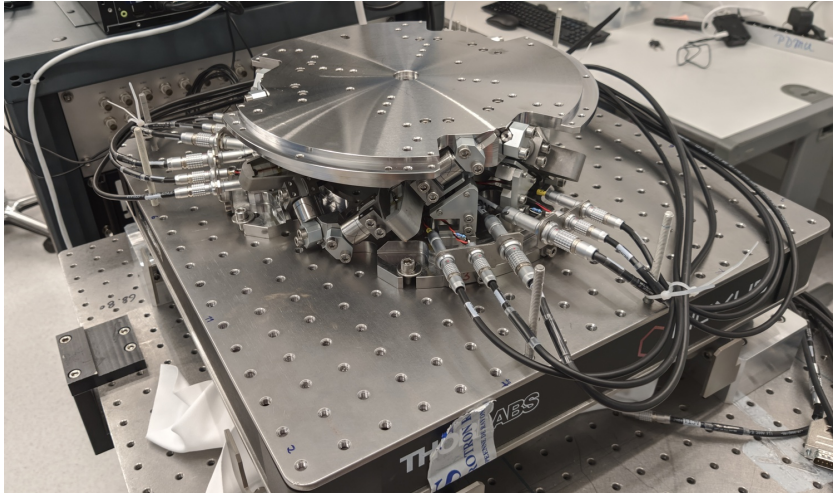


**Figure 3.1:** Mounted Nano-Hexapod on top of the suspended table

A modal analysis of the nano-hexapod is first performed in Section 3.1. The results of the modal analysis will be useful to better understand the measured dynamics from actuators to sensors.

A block diagram of the (open-loop) system is shown in Figure 3.2. The frequency response functions from controlled signals  $\mathbf{u}$  to the force sensors voltages  $\mathbf{V}_s$  and to the encoders measured displacements  $\mathbf{d}_e$  are experimentally identified in Section 3.2. The effect of the payload mass on the dynamics is discussed in Section 3.3.

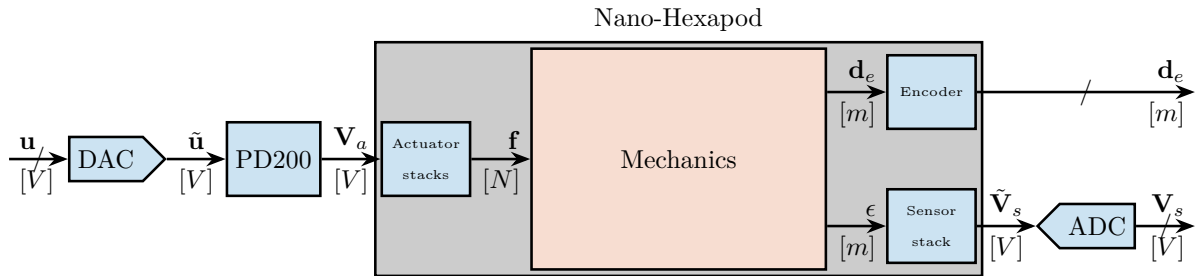


**Figure 3.2:** Block diagram of the studied system. The command signal generated by the speedgoat is  $\mathbf{u}$ , and the measured signals are  $\mathbf{d}_e$  and  $\mathbf{V}_s$ . Units are indicated in square brackets.

## 3.1 Modal analysis

To facilitate the future analysis of the measured plant dynamics, a basic modal analysis of the nano-hexapod is performed. Five 3-axis accelerometers were fixed on the top platform of the nano-hexapod (Figure 3.3) and the top platform was excited using an instrumented hammer.

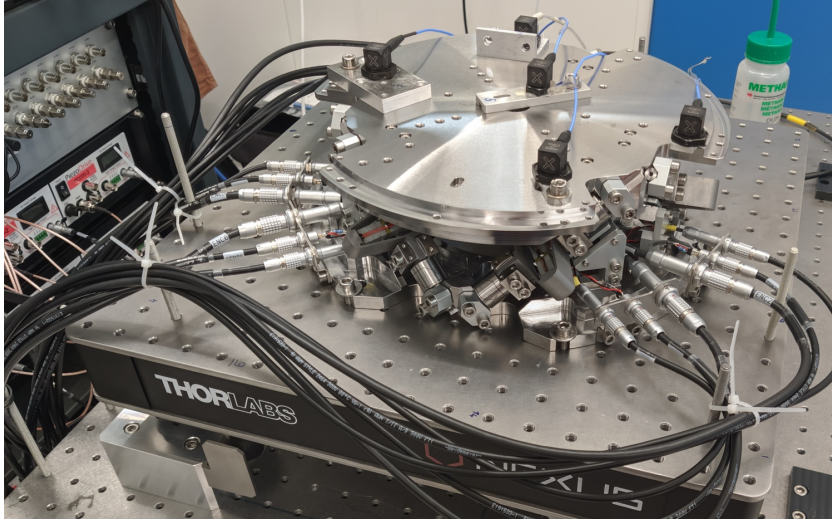


**Figure 3.3:** Five accelerometers fixed on top of the nano-hexapod to perform a modal analysis

Between 100Hz and 200Hz, 6 suspension modes (i.e. rigid body modes of the top platform) were identified. At around 700Hz, two flexible modes of the top plate were observed (see Figure 3.4). These modes are summarized in Table 3.1.

**Table 3.1:** Description of the identified modes of the Nano-Hexapod

Mode	Frequency	Description
1	120 Hz	Suspension Mode: Y-translation
2	120 Hz	Suspension Mode: X-translation
3	145 Hz	Suspension Mode: Z-translation
4	165 Hz	Suspension Mode: Y-rotation
5	165 Hz	Suspension Mode: X-rotation
6	190 Hz	Suspension Mode: Z-rotation
7	692 Hz	(flexible) Membrane mode of the top platform
8	709 Hz	Second flexible mode of the top platform

## 3.2 Identification of the dynamics

The dynamics of the nano-hexapod from the six command signals ( $u_1$  to  $u_6$ ) to the six measured displacement by the encoders ( $d_{e1}$  to  $d_{e6}$ ) and to the six force sensors ( $V_{s1}$  to  $V_{s6}$ ) were identified by generating low-pass filtered white noise for each command signal, one by one.

The  $6 \times 6$  FRF matrix from  $\mathbf{u}$  to  $\mathbf{d}_e$  is shown in Figure 3.5. The diagonal terms are displayed using colored lines, and all the 30 off-diagonal terms are displayed by gray lines.

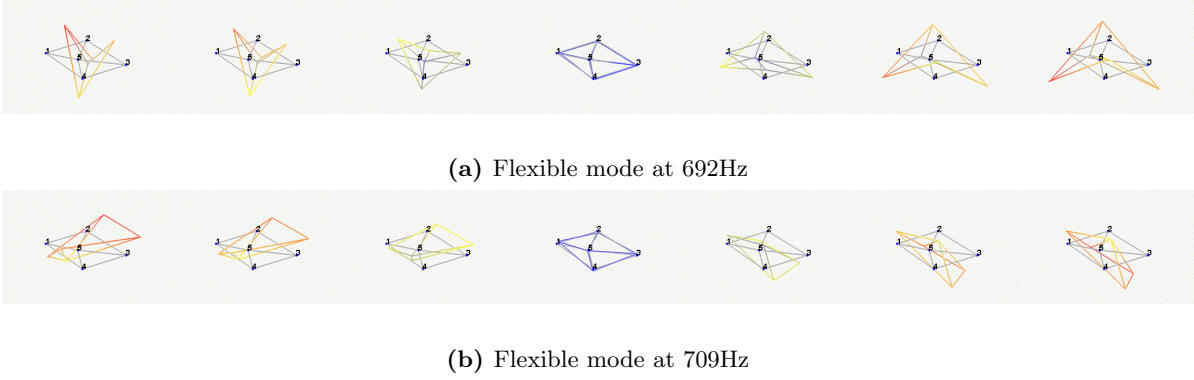


**Figure 3.4:** Two identified flexible modes of the top plate of the Nano-Hexapod

All six diagonal terms are well superimposed up to at least  $1\text{ kHz}$ , indicating good manufacturing and mounting uniformity. Below the first suspension mode, good decoupling can be observed (the amplitude of all off-diagonal terms are  $\approx 20$  times smaller than the diagonal terms), indicating the correct assembly of all parts.

From  $10\text{ Hz}$  up to  $1\text{ kHz}$ , around 10 resonance frequencies can be observed. The first 4 are suspension modes (at  $122\text{ Hz}$ ,  $143\text{ Hz}$ ,  $165\text{ Hz}$  and  $191\text{ Hz}$ ) which correlate the modes measured during the modal analysis in Section 3.1. Three modes at  $237\text{ Hz}$ ,  $349\text{ Hz}$  and  $395\text{ Hz}$  are attributed to the internal strut resonances (this will be checked in Section 4.2). Except for the mode at  $237\text{ Hz}$ , their impact on the dynamics is small. The two modes at  $665\text{ Hz}$  and  $695\text{ Hz}$  are attributed to the flexible modes of the top platform. Other modes can be observed above  $1\text{ kHz}$ , which can be attributed to flexible modes of the encoder supports or to flexible modes of the top platform.

Up to at least  $1\text{ kHz}$ , an alternating pole/zero pattern is observed, which makes the control easier to tune. This would not have occurred if the encoders were fixed to the struts.

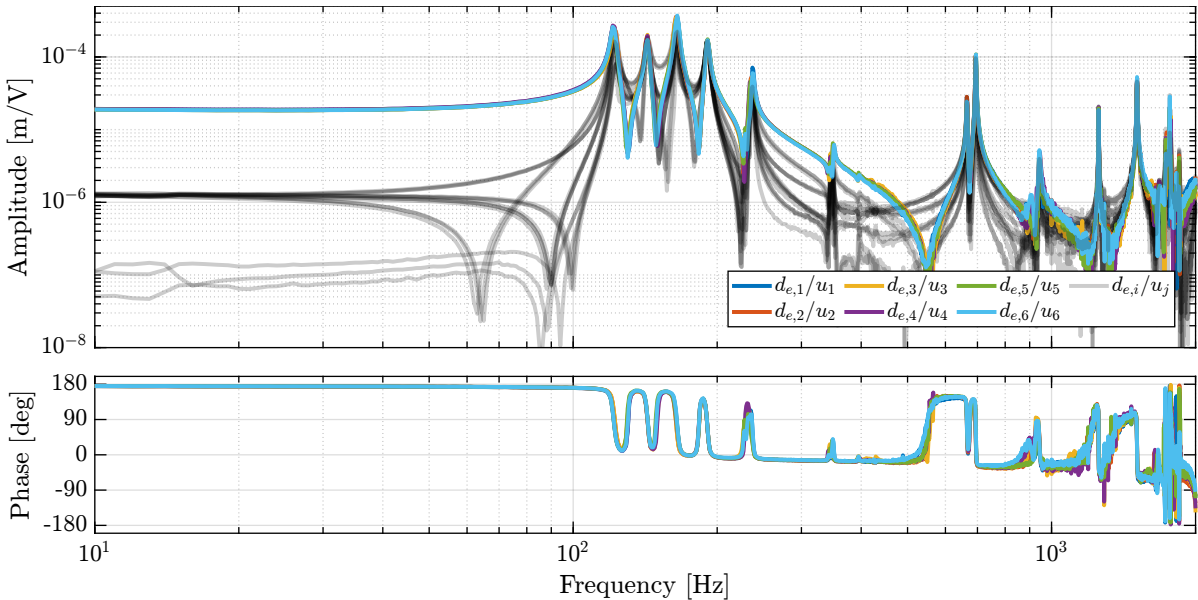


**Figure 3.5:** Measured FRF for the transfer function from  $\mathbf{u}$  to  $\mathbf{d}_e$ . The 6 diagonal terms are the colored lines (all superimposed), and the 30 off-diagonal terms are the gray lines.

Similarly, the  $6 \times 6$  FRF matrix from  $\mathbf{u}$  to  $\mathbf{V}_s$  is shown in Figure 3.6. Alternating poles and zeros can be observed up to at least 2kHz, which is a necessary characteristics for applying decentralized IFF. Similar to what was observed for the encoder outputs, all the “diagonal” terms are well superimposed, indicating that the same controller can be applied to all the struts. The first flexible mode of the struts as 235Hz has large amplitude, and therefore, it should be possible to add some damping to this mode using IFF.

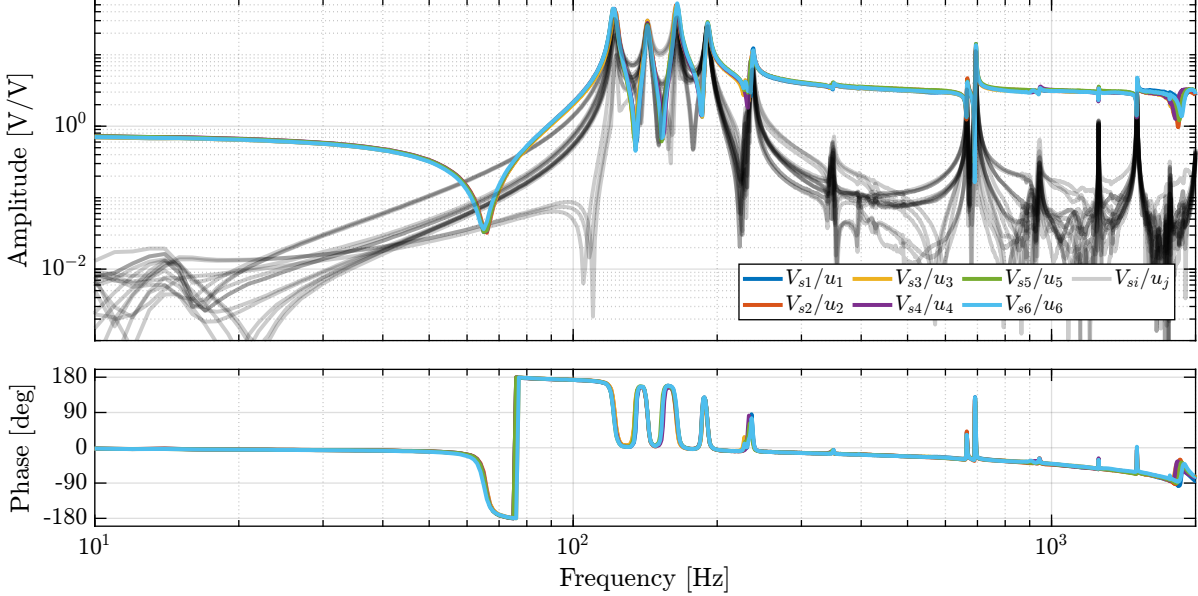


**Figure 3.6:** Measured FRF for the transfer function from  $\mathbf{u}$  to  $\mathbf{V}_s$ . The 6 diagonal terms are the colored lines (all superimposed), and the 30 off-diagonal terms are the shaded black lines.

### 3.3 Effect of payload mass on the dynamics

One major challenge for controlling the NASS is the wanted robustness to a variation of payload mass; therefore, it is necessary to understand how the dynamics of the nano-hexapod changes with a change in payload mass.

To study how the dynamics changes with the payload mass, up to three “cylindrical masses” of 13 kg each can be added for a total of  $\approx 40$  kg. These three cylindrical masses on top of the nano-hexapod are shown in Figure 3.7.

The obtained frequency response functions from actuator signal  $u_i$  to the associated encoder  $d_{ei}$  for the four payload conditions (no mass, 13kg, 26kg and 39kg) are shown in Figure 3.8a. As expected, the frequency of the suspension modes decreased with increasing payload mass. The low frequency gain does not change because it is linked to the stiffness property of the nano-hexapod and not to its mass property.

The frequencies of the two flexible modes of the top plate first decreased significantly when the first mass was added (from  $\approx 700$  Hz to  $\approx 400$  Hz). This is because the added mass is composed of two half cylinders that are not fixed together. Therefore, it adds a lot of mass to the top plate without increasing stiffness in one direction. When more than one “mass layer” is added, the half cylinders are added at some angles such that rigidity is added in all directions (see how the three mass “layers” are

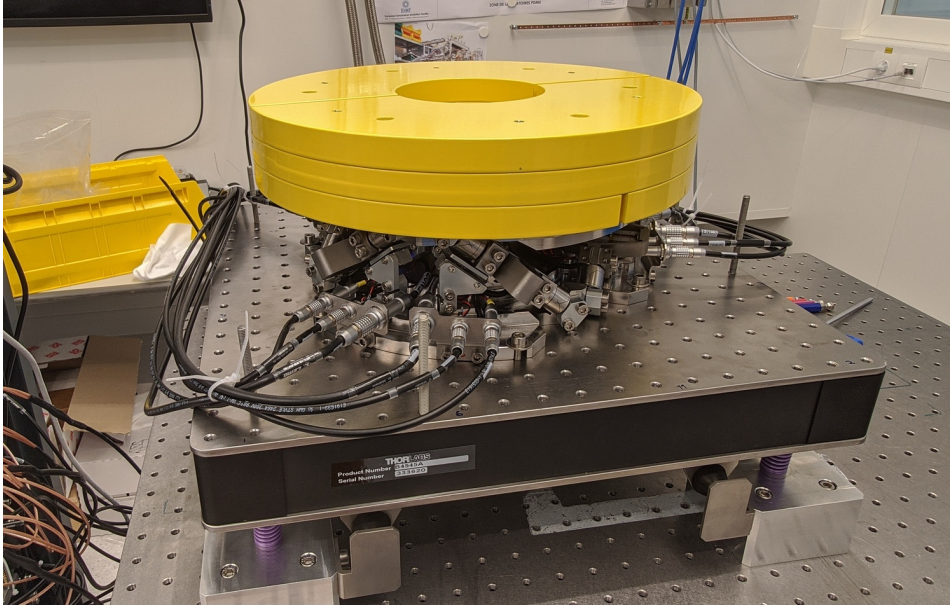


**Figure 3.7:** Picture of the nano-hexapod with the added three cylindrical masses for a total of  $\approx 40\text{ kg}$

positioned in Figure 3.7). In this case, the frequency of these flexible modes is increased. In practice, the payload should be one solid body, and no decrease in the frequency of this flexible mode should be observed. The apparent amplitude of the flexible mode of the strut at 237Hz becomes smaller as the payload mass increased.

The measured FRFs from  $u_i$  to  $V_{si}$  are shown in Figure 3.8b. For all tested payloads, the measured FRF always have alternating poles and zeros, indicating that IFF can be applied in a robust manner.

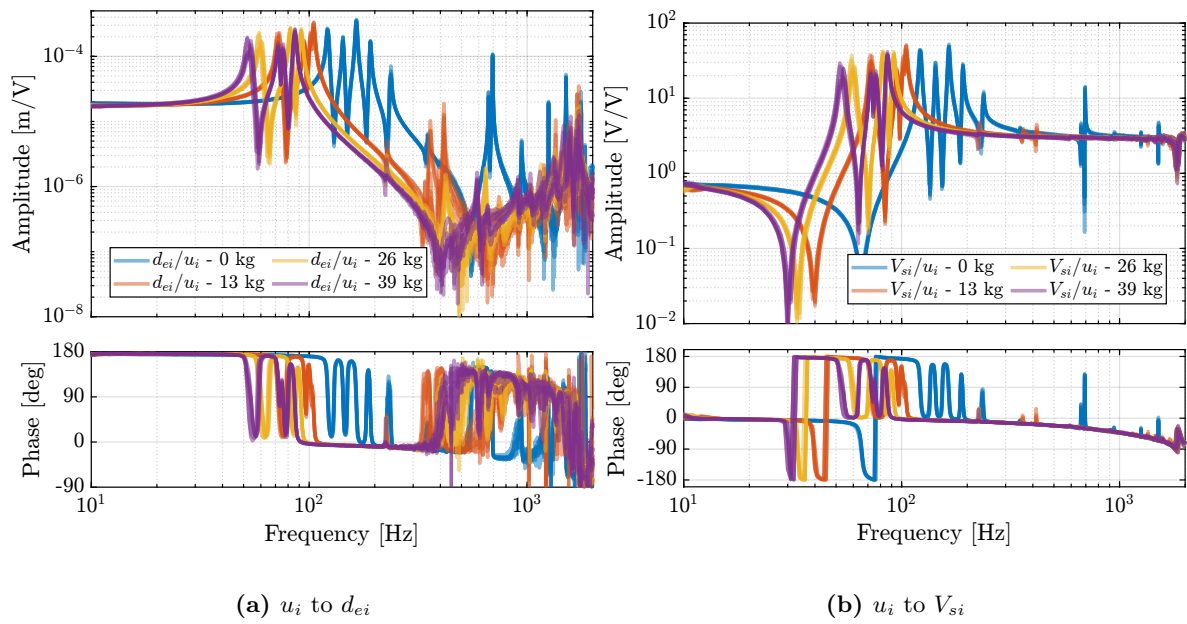


**Figure 3.8:** Measured Frequency Response Functions from  $u_i$  to  $d_{ei}$  (a) and from  $u_i$  to  $V_{si}$  (b) for all 4 payload conditions. Only diagonal terms are shown.

## 4 Nano-Hexapod Model Dynamics

In this section, the dynamics measured in Section 3 is compared with those estimated from the multi-body model. The nano-hexapod multi-body model was therefore added on top of the vibration table multi-body model, as shown in Figure 4.1.

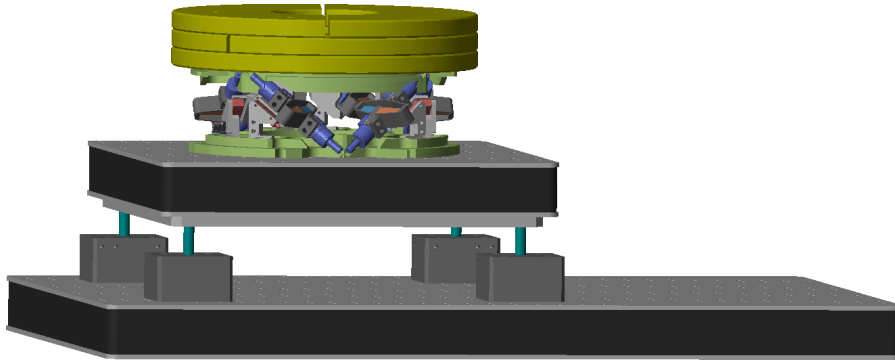


**Figure 4.1:** 3D representation of the multi-body model with the nano-hexapod on top of the suspended table. Three mass “layers” are here added

The model should exhibit certain characteristics that are verified in this section. First, it should match the measured system dynamics from actuators to sensors presented in Section 3. Both the “direct” terms (Section 4.1) and “coupling” terms (Section 4.2) of the multi-body model are compared with the measured dynamics. Second, it should also represent how the system dynamics changes when a payload is fixed to the top platform. This is checked in Section 4.3.

### 4.1 Nano-Hexapod model dynamics

The multi-body model of the nano-hexapod was first configured with 4-DoF flexible joints, 2-DoF APA, and rigid top and bottom plates. The stiffness values of the flexible joints were chosen based on the values estimated using the test bench and on the FEM. The parameters of the APA model were determined from the test bench of the APA. The  $6 \times 6$  transfer function matrices from  $\mathbf{u}$  to  $\mathbf{d}_e$  and from  $\mathbf{u}$  to  $\mathbf{V}_s$  are then extracted from the multi-body model.

First, it is evaluated how well the model matches the “direct” terms of the measured FRF matrix. To do so, the diagonal terms of the extracted transfer function matrices are compared with the measured FRF in Figure 4.2. It can be seen that the 4 suspension modes of the nano-hexapod (at 122Hz, 143Hz, 165Hz and 191Hz) are well modeled. The three resonances that were attributed to “internal” flexible modes of the struts (at 237Hz, 349Hz and 395Hz) cannot be seen in the model, which is reasonable because the APAs are here modeled as a simple uniaxial 2-DoF system. At higher frequencies, no

resonances can be observed in the model, as the top plate and the encoder supports are modeled as rigid bodies.

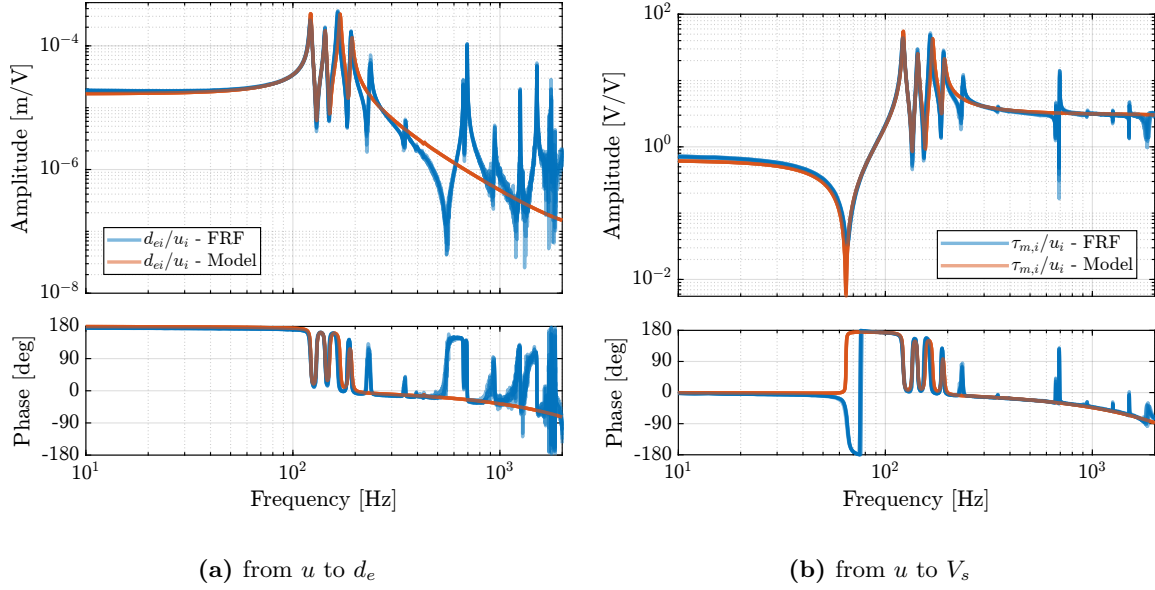


**Figure 4.2:** Comparison of the diagonal elements (i.e. “direct” terms) of the measured FRF matrix and the dynamics identified from the multi-body model. Both for the dynamics from  $u$  to  $d_e$  (a) and from  $u$  to  $V_s$  (b)

## 4.2 Dynamical coupling

Another desired feature of the model is that it effectively represents coupling in the system, as this is often the limiting factor for the control of MIMO systems. Instead of comparing the full  $6 \times 6$  FRF matrix from  $\mathbf{u}$  to  $\mathbf{d}_e$ , only the first “column” is compared (Figure 4.3), which corresponds to the transfer function from the command  $u_1$  to the six measured encoder displacements  $d_{e1}$  to  $d_{e6}$ . It can be seen that the coupling in the model matches the measurements well up to the first un-modeled flexible mode at 237Hz. Similar results are observed for all other coupling terms and for the transfer function from  $\mathbf{u}$  to  $\mathbf{V}_s$ .

The APA300ML was then modeled with a *super-element* extracted from a FE-software. The obtained transfer functions from  $u_1$  to the six measured encoder displacements  $d_{e1}$  to  $d_{e6}$  are compared with the measured FRF in Figure 4.4. While the damping of the suspension modes for the *super-element* is underestimated (which could be solved by properly tuning the proportional damping coefficients), the flexible modes of the struts at 237Hz and 349Hz are well modeled. Even the mode 395Hz can be observed in the model. Therefore, if the modes of the struts are to be modeled, the *super-element* of the APA300ML can be used at the cost of obtaining a much higher order model.

## 4.3 Effect of payload mass

Another important characteristic of the model is that it should represent the dynamics of the system well for all considered payloads. The model dynamics is therefore compared with the measured dynamics

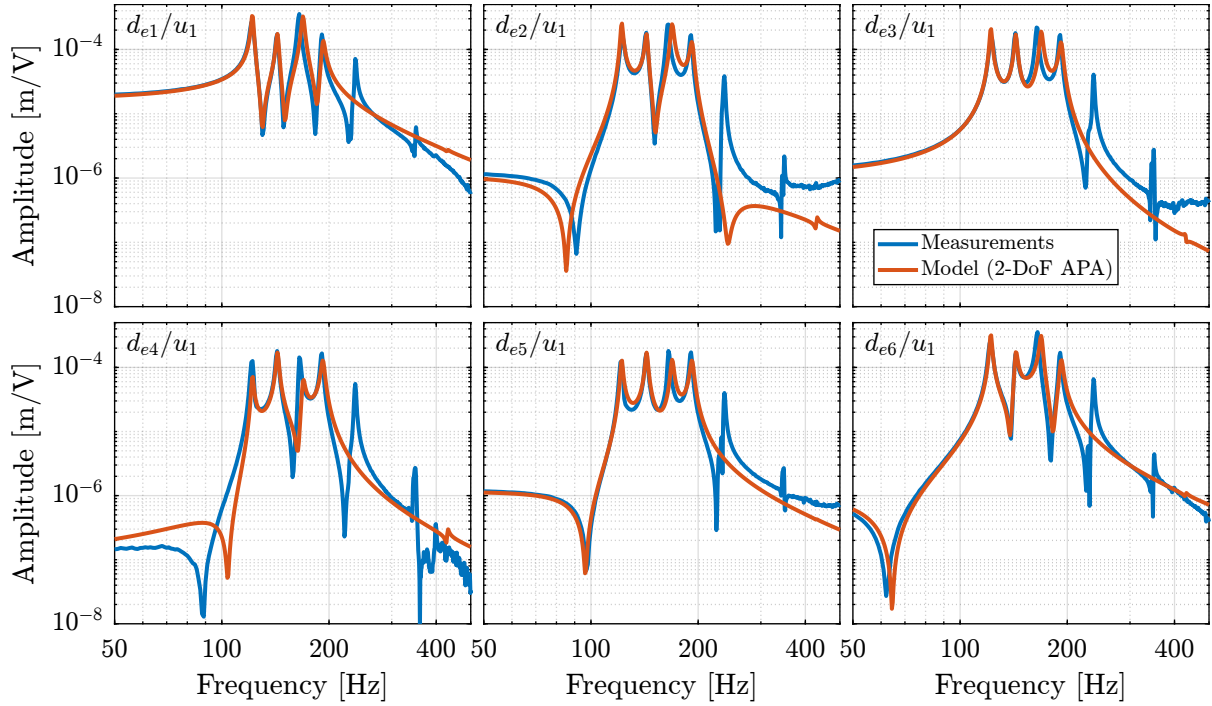


**Figure 4.3:** Comparison of the measured (in blue) and modeled (in red) frequency transfer functions from the first control signal  $u_1$  to the six encoders  $d_{e_1}$  to  $d_{e_6}$ . The APA are here modeled with a 2-DoF mass-spring-damper system.

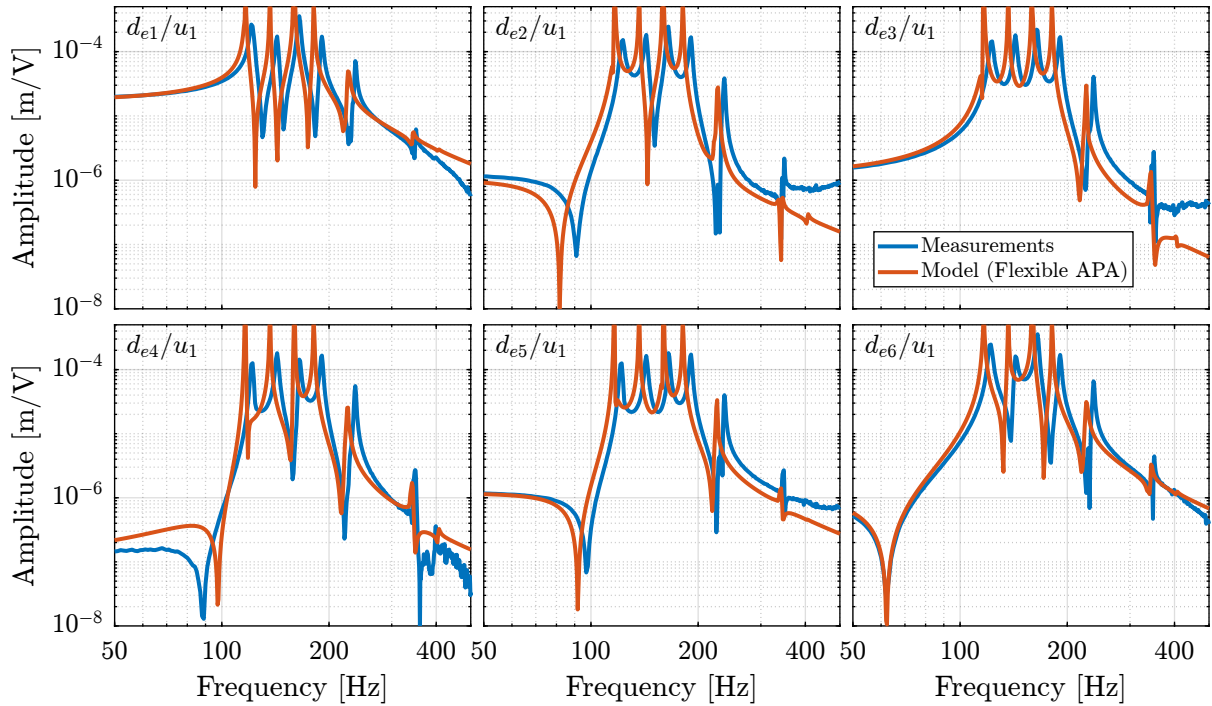


**Figure 4.4:** Comparison of the measured (in blue) and modeled (in red) frequency transfer functions from the first control signal  $u_1$  to the six encoders  $d_{e_1}$  to  $d_{e_6}$ . The APA are here modeled with a “super-element”.

for 4 payloads (no payload, 13kg, 26kg and 39kg) in Figure 4.5. The observed shift of the suspension modes to lower frequencies with increased payload mass is well represented by the multi-body model. The complex conjugate zeros also well match the experiments both for the encoder outputs (Figure 4.5a) and the force sensor outputs (Figure 4.5b).

Note that the model displays smaller damping than that observed experimentally for high values of the payload mass. One option could be to tune the damping as a function of the mass (similar to what is done with the Rayleigh damping). However, as decentralized IFF will be applied, the damping is actively brought, and the open-loop damping value should have very little impact on the obtained plant dynamics.

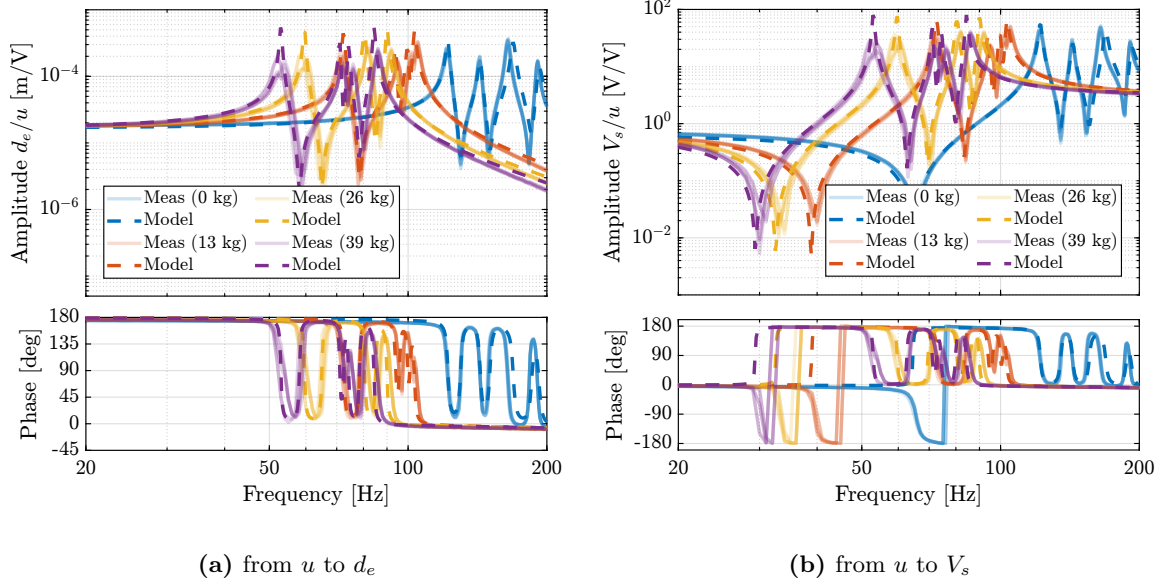


**Figure 4.5:** Comparison of the diagonal elements (i.e. “direct” terms) of the measured FRF matrix and the dynamics identified from the multi-body model. Both for the dynamics from  $u$  to  $d_e$  (a) and from  $u$  to  $V_s$  (b)

In order to also check if the model well represents the coupling when high payload masses are used, the transfer functions from  $u_1$  to  $d_{e1}$  to  $d_{e6}$  are compared in the case of the 39kg payload in Figure 4.6. Excellent match between experimental and model coupling is observed. Therefore, the model effectively represents the system coupling for different payloads.

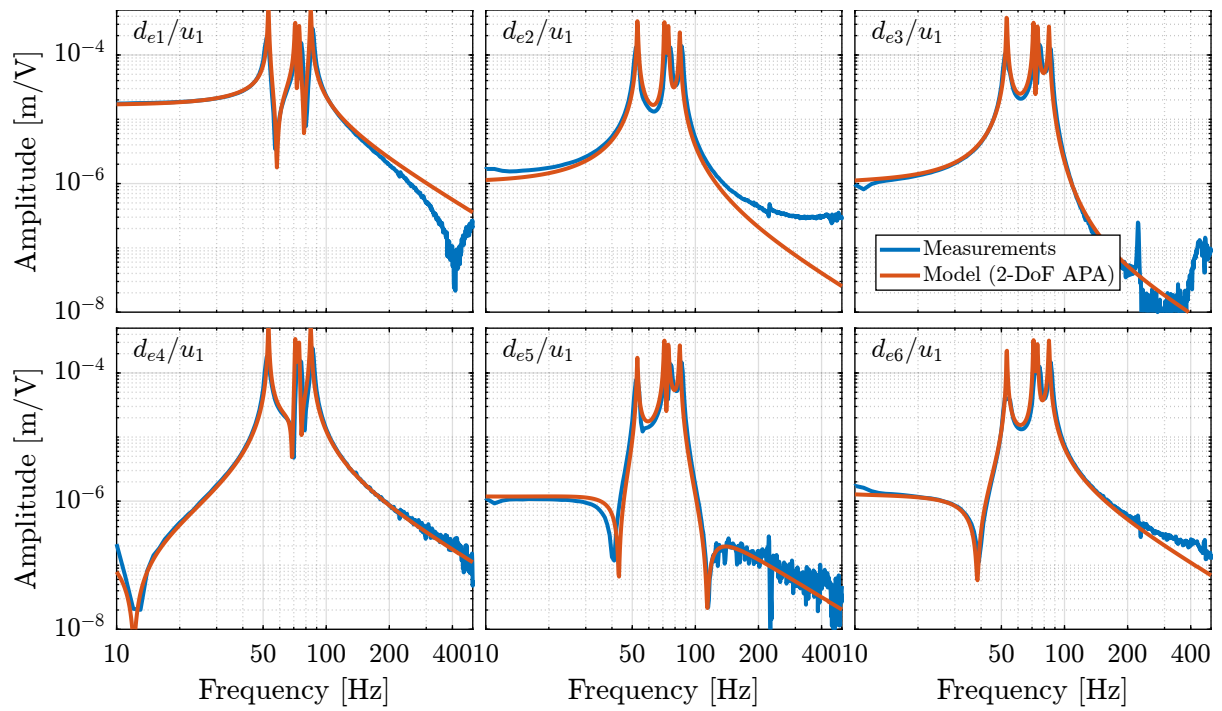


**Figure 4.6:** Comparison of the measured (in blue) and modeled (in red) frequency transfer functions from the first control signal  $u_1$  to the six encoders  $d_{e1}$  to  $d_{e6}$

## 5 Conclusion

The goal of this test bench was to obtain an accurate model of the nano-hexapod that could then be included on top of the micro-station model. The adopted strategy was to identify the nano-hexapod dynamics under conditions in which all factors that could have affected the nano-hexapod dynamics were considered. This was achieved by developing a suspended table with low frequency suspension modes that can be accurately modeled (Section 2). Although the dynamics of the nano-hexapod was indeed impacted by the dynamics of the suspended platform, this impact was also considered in the multi-body model.

The dynamics of the nano-hexapod was then identified in Section 3. Below the first suspension mode, good decoupling could be observed for the transfer function from  $\mathbf{u}$  to  $\mathbf{d}_e$ , which enables the design of a decentralized positioning controller based on the encoders for relative positioning purposes. Many other modes were present above 700Hz, which will inevitably limit the achievable bandwidth. The observed effect of the payload’s mass on the dynamics was quite large, which also represents a complex control challenge.

The frequency response functions from the six DAC voltages  $\mathbf{u}$  to the six force sensors voltages  $\mathbf{V}_s$  all have alternating complex conjugate poles and complex conjugate zeros for all the tested payloads (Figure 4.5b). This indicates that it is possible to implement decentralized Integral Force Feedback in a robust manner.

The developed multi-body model of the nano-hexapod was found to accurately represents the suspension modes of the Nano-Hexapod (Section 4). Both FRF matrices from  $\mathbf{u}$  to  $\mathbf{V}_s$  and from  $\mathbf{u}$  to  $\mathbf{d}_e$  are well matching with the measurements, even when considering coupling (i.e. off-diagonal) terms, which are very important from a control perspective. At frequencies above the suspension modes, the Nano-Hexapod model became inaccurate because the flexible modes were not modeled. It was found that modeling the APA300ML using a *super-element* allows to model the internal resonances of the struts. The same can be done with the top platform and the encoder supports; however, the model order would be higher and may become unpractical for simulation.

Obtaining a model that accurately represents the complex dynamics of the Nano-Hexapod was made possible by the modeling approach used in this study. This approach involved tuning and validating models of individual components (such as the APA and flexible joints) using dedicated test benches. The different models could then be combined to form the Nano-Hexapod dynamical model. If a model of the nano-hexapod was developed in one time, it would be difficult to tune all the model parameters to match the measured dynamics, or even to know if the model “structure” would be adequate to represent the system dynamics.